NUMERICAL INVESTIGATION OF SUPERSONIC FLOW SEPARATION IN THRUST-OPTIMIZED CONTOUR ROCKET NOZZLE

Bensayah Khaled[1,2*] and Kamri Khadidja[2]

[1] Interprofessional Complex Research in Aerothermochemistry CORIA UMR 6614 CNRS,
  INSA of Rouen, France
   e-mail: k.bensayah@lagh-univ.dz
[2] Laboratory of Mechanic, department of mechanical engineering, University of Laghouat,
  Algeria
   e-mail: kha.kamri@yahoo.com
  corresponding author

Abstract

The difficulties associated with thrust-optimized contour nozzles have led to significant advances in our knowledge of the physical phenomena associated with flow separation. In this study, a fully implicit scheme is implemented using a combined weight function for splitting the flux to analyze the shock patterns in the optimized contour (TOC) that occur during the process of separation, leading to free (FSS) or restricted (RSS) shock separation. The switching FSS/RSS hysteresis at startup and shutdown is also investigated. To better understand and validate the findings and study the properties of the oscillating flow during the start-up procedure, an axisymmetric two-dimensional numerical simulation was performed for the TOC nozzle. A code was developed to solve the unsteady Navier-Stokes equations for compressible nozzle flow with boundary layer/shock wave interactions with the implementation of a full RSM-Omega turbulence model. These findings were used to analyze the separation structures, shock wave interactions, and hysteresis phenomena.

Keywords: Hysteresis**,** RSM-Omega turbulence modeling, explicit-implicit scheme, free shock separation, restricted shock separation

1. Introduction

Supersonic nozzle flow separation is associated with oblique shock required to deflect the supersonic jet flow and build up pressure to match the environmental conditions. The detachment shock is consistently reflected on the axis nozzle with Mach reflection. Depending on the parameters of the upstream flow, this Mach reflection might exhibit a curved or flat Mach disk. For optimized contour nozzles, the Mack disk is curved due to the significant radial gradients of the flow in front of it, resulting from the internal shock generated by the throat. The rocket engines in current launchers and missiles are designed to reach full flowing at sea level.

The boundary layer separation of nozzle flow has been the objective of numerous experimental and numerical investigations, because the performance of rocket motors depends

strongly on the expansion nozzle's aerodynamic design and the contour form, and the expansion cross-section ratio of the engine are two primary factors in thrust nozzle optimization.

The area ratio limit is determined with the maximum lateral force that can be tolerated when operating under these off-design conditions because of instability and symmetry loss of nozzle separated flow. Computational and experimental studies of side loads and separated flow in TOC nozzles have already been conducted. The re-attachment of flow behind the RSS detachment, associated with intense lateral vibrations, was initially described by the cold experimental data of Nave and Coffey (1973) in the 1970s on the J-2S nozzle. This shows the presence of two distinct flow patterns: free shock separation, where the boundary layer is separated and not reattached to the wall nozzle, and the RSS restricted shock separation distinguished by recirculating bubbles with nozzle wall re-attachment. In the study by Chen et al. (1994), numerical simulations on a subscale J-2S engine demonstrated the existence of flow reattachment (RSS) and the existence of a trapped vortex.

In a paper published by Frey and Hagemann (1998), the focus was on RSS flow structure recovered through numerical simulations. Nasuti and Onofri (1996) demonstrated by numerical simulations the effect of the vortex in deflecting the central flow towards the walls. An analytical model for the cap shock structure associated with the RSS phase and for FSS-RSS transition prediction was provided by Frey et al. (2017). Reverse flow in TOC nozzle plume has latterly been experimentally demonstrated (Wang et al. (2013), Stark and Génin (2016), Steger and Warming (1979)).

A Fortran code was developed to analyze numerical simulations in order to comprehend how shock interactions affect the separation model. The analysis establishes an accurate understanding of fluid flow physics as well as the impact of hysteresis occurring at the start-up transition.

2. Turbulence model and numerical method

The equations of the Reynolds stress model RSM-ω for the transport of the Reynolds stresses $\bar{\rho} R_{ij} = -\overline{\rho u_i'' u_j''}$ are given by:

$$\frac{\partial \bar{\rho} R_{ij}}{\partial t} + \frac{\partial \left(\bar{\rho} U_k R_{ij} \right)}{\partial x_k} = P_{ij} + \Pi_{ij} - \frac{2}{3} \beta^* f_{\beta^*} \bar{\rho} \omega k \delta_{ij} + \frac{\partial}{\partial x_k} \left[\left(\mu + \frac{\mu_t}{\sigma_k} \right) \frac{\partial R_{ij}}{\partial x_k} \right] \tag{1}$$

$$\frac{\partial \bar{\rho} \omega}{\partial t} + \frac{\partial \left(\bar{\rho} U_k \omega \right)}{\partial x_k} = \frac{\alpha \bar{\rho} \omega}{k} R_{ij} \frac{\partial U_i}{\partial x_j} - \bar{\rho} \beta f_{\beta} \omega^2 + \frac{\partial}{\partial x_k} \left[\left(\mu + \frac{\mu_t}{\sigma} \right) \frac{\partial \omega}{\partial x_k} \right] + \sigma_d \frac{\bar{\rho}}{\omega} \frac{\partial k}{\partial x_j} \frac{\partial \omega}{\partial x_j} \tag{2}$$

The pressure-strain correlation is given by

$$\Pi_{ij} = \beta^* C_1 \bar{\rho} \omega \left(R_{ij} + \frac{2}{3} k \delta_{ij} \right) - \hat{\alpha} \left(P_{ij} - \frac{2}{3} P \delta_{ij} \right) - \hat{\beta} \left(D_{ij} - \frac{2}{3} P \delta_{ij} \right) - \hat{\gamma} \bar{\rho} k \left(S_{ij} - \frac{1}{3} S_{kk} \delta_{ij} \right) \tag{3}$$

The production tensor P_{ij} and the tensor D_{ij} are given by:

$$P_{ij} = -\overline{\rho u_i'' u_k''} \frac{\partial U_j}{\partial x_k} - \overline{\rho u_j'' u_k''} \frac{\partial U_i}{\partial x_k}, \quad D_{ij} = -\overline{\rho u_i'' u_k''} \frac{\partial U_k}{\partial x_j} - \overline{\rho u_j'' u_k''} \frac{\partial U_k}{\partial x_i} \tag{4}$$

With $k = -R_{ii}/2$, $\mu_t = \bar{\rho} k / \omega$ and $P = P_{kk}/2$.

In generalized coordinates, the system of equations in conserved form is done as:

$$\frac{\partial U}{\partial t} + \frac{\partial F}{\partial \xi} + \frac{\partial G}{\partial \eta} + \frac{\partial F_v}{\partial \xi} + \frac{\partial G_v}{\partial \eta} = S(U)$$

$$U = \left(\bar{\rho}, \bar{\rho}U, \bar{\rho}V, \bar{\rho}E, \bar{\rho}\overline{u''v''}, \bar{\rho}\overline{u''u''}, \bar{\rho}\overline{v''v''}, \bar{\rho}\overline{w''w''}, \bar{\rho}\omega \right)^T$$

(5)

F, G and F_v, G_v are respectively the inviscid flux and the viscous vectors. With $V_{ij} = dv$ is the elementary volume of the integration mesh ij; $|J\Delta\xi| = \sqrt{(J\xi_x)^2 + (J\xi_y)^2}$ taken on the segment $\xi = Cste$ between η and $\eta+1$. $n_x = (J\xi_x)/|J\Delta\xi|$ and $n_y = (J\xi_y)/|J\Delta\xi|$ correspond to the direct cosines of its external norm $\vec{\xi}$ directed in the direction of the increasing ξ. $\tilde{U} = \tilde{u}n_x + \tilde{v}n_y$ can be interpreted as the flow velocity passing through it, measured according to $\vec{\xi}$, the same interpretation is done for m_x, m_y and for $\tilde{V} = \tilde{u}m_x + \tilde{v}m_y$ with J is the Jacobian of a fictitious cell built on the four points used in the estimation of the derivatives.

$$F_{i-\frac{1}{2}} = \frac{|J\Delta\xi|}{V_{ij}} \begin{pmatrix} \bar{\rho}U \\ \bar{\rho}UU + \bar{p}n_x + \bar{\rho}\overline{u''u''} \\ \bar{\rho}UV + \bar{p}n_y + \bar{\rho}\overline{u''v''} \\ \left(\bar{\rho}E + \bar{p} + \bar{\rho}\overline{u''u''}\right)U + \bar{\rho}\overline{u''v''}V \\ \bar{\rho}\overline{u''v''}U \\ \bar{\rho}\overline{u''u''}U \\ \bar{\rho}\overline{v''v''}U \\ \bar{\rho}\overline{w''w''}U \\ \bar{\rho}\omega U \end{pmatrix} , \quad G_{j-\frac{1}{2}} = \frac{|J\Delta\eta|}{V_{ij}} \begin{pmatrix} \bar{\rho}V \\ \bar{\rho}VU + \bar{p}m_x + \bar{\rho}\overline{u''v''} \\ \bar{\rho}VV + \bar{p}m_y + \bar{\rho}\overline{v''v''} \\ \left(\bar{\rho}E + \bar{p} + \bar{\rho}\overline{v''v''}\right)V + \overline{\bar{\rho}u''v''U} \\ \overline{\bar{\rho}u''v''V} \\ \overline{\bar{\rho}u''u''V} \\ \overline{\bar{\rho}v''v''V} \\ \overline{\bar{\rho}w''w''V} \\ \overline{\bar{\rho}\omega V} \end{pmatrix}$$

(6)

$$\frac{V_{ij}F_{vi-\frac{1}{2}}}{\left|J\Delta\xi\right|} = \begin{pmatrix} f_{v1} = 0 \\ f_{v2} = -\tau_{xx}n_x - \tau_{xy}n_y \\ f_{v3} = -\tau_{yx}n_x - \tau_{yy}n_y \\ \\ f_{v4} = \tilde{u}f_{v2} + \tilde{v}f_{v3} - \mu_T\left(n_x\frac{\partial\tilde{T}}{\partial x} + n_y\frac{\partial\tilde{T}}{\partial y}\right) \\ \\ f_{v5} = -\mu\overline{u''v''}\left(n_x\frac{\partial\overline{u''v''}}{\partial x} + n_y\frac{\partial\overline{u''v''}}{\partial y}\right) \\ \\ f_{v6} = -\mu\overline{u''u''}\left(n_x\frac{\partial\overline{u''u''}}{\partial x} + n_y\frac{\partial\overline{u''u''}}{\partial y}\right) \\ \\ f_{v7} = -\mu\overline{v''v''}\left(n_x\frac{\partial\overline{v''v''}}{\partial x} + n_y\frac{\partial\overline{v''v''}}{\partial y}\right) \\ \\ f_{v8} = -\mu\overline{w''w''}\left(n_x\frac{\partial\overline{w''w''}}{\partial x} + n_y\frac{\partial\overline{w''w''}}{\partial y}\right) \\ \\ f_{v9} = -\mu\tilde{\omega}\left(n_x\frac{\partial\tilde{\omega}}{\partial x} + n_y\frac{\partial\tilde{\omega}}{\partial y}\right) \end{pmatrix}, \quad \frac{V_{ij}G_{vj-\frac{1}{2}}}{\left|J\Delta\eta\right|} = \begin{pmatrix} g_{v1} = 0 \\ g_{v2} = -\tau_{xx}m_x - \tau_{xy}m_y \\ g_{v3} = -\tau_{yx}m_x - \tau_{yy}m_y \\ \\ g_{v4} = \tilde{u}g_{v2} + \tilde{v}g_{v3} - \mu_T\left(m_x\frac{\partial\tilde{T}}{\partial x} + m_y\frac{\partial\tilde{T}}{\partial y}\right) \\ \\ g_{v5} = -\mu\overline{u''v''}\left(m_x\frac{\partial\overline{u''v''}}{\partial x} + m_y\frac{\partial\overline{u''v''}}{\partial y}\right) \\ \\ g_{v6} = -\mu\overline{u''u''}\left(m_x\frac{\partial\overline{u''u''}}{\partial x} + m_y\frac{\partial\overline{u''u''}}{\partial y}\right) \\ \\ g_{v7} = -\mu\overline{v''v''}\left(m_x\frac{\partial\overline{v''v''}}{\partial x} + m_y\frac{\partial\overline{v''v''}}{\partial y}\right) \\ \\ g_{v8} = -\mu\overline{w''w''}\left(m_x\frac{\partial\overline{w''w''}}{\partial x} + m_y\frac{\partial\overline{w''w''}}{\partial y}\right) \\ \\ g_{v9} = -\mu\tilde{\omega}\left(m_x\frac{\partial\tilde{\omega}}{\partial x} + m_y\frac{\partial\tilde{\omega}}{\partial y}\right) \end{pmatrix} \tag{7}$$

The pressure is done by $p = (\gamma - 1)\bar{\rho}\left(\tilde{E} - (\tilde{U}^2 + \tilde{V}^2)/2 - k\right)$, the viscosity is done by the Sutherland's law. Equation 5 can be integrated using Green's theorem in a small volume.

$$\frac{\partial U}{\partial t} + \frac{1}{dv}\int_{dv}\left(\frac{\partial F}{\partial x} + \frac{\partial G}{\partial y}\right)dv = \frac{1}{dv}\int_{dv}\left(\frac{\partial F_v}{\partial x} + \frac{\partial G_v}{\partial y}\right)dv + S \tag{8}$$

The equation 8 can be written in generalized coordinates as:

$$\frac{\partial U_{i,j}}{\partial t} + \frac{1}{V_{i,j}}\left(FS_{ixp} + GS_{iyp}\right)_{i+\frac{1}{2},j}\left|\vec{S}_{i+\frac{1}{2}}\right| - \frac{1}{V_{i,j}}\left(FS_{ixp} + GS_{iyp}\right)_{i-\frac{1}{2},j}\left|\vec{S}_{i-\frac{1}{2}}\right| +$$
$$\frac{1}{V_{i,j}}\left(FS_{jxp} + GS_{jyp}\right)_{i,j+\frac{1}{2}}\left|\vec{S}_{j+\frac{1}{2}}\right| - \frac{1}{V_{i,j}}\left(FS_{jxp} + GS_{jyp}\right)_{i,j-\frac{1}{2}}\left|\vec{S}_{j-\frac{1}{2}}\right| =$$
$$\frac{1}{V_{i,j}}\left(F_v S_{ixp} + G_v S_{iyp}\right)_{i+\frac{1}{2},j}\left|\vec{S}_{i+\frac{1}{2}}\right| - \frac{1}{V_{i,j}}\left(F_v S_{ixp} + G_v S_{iyp}\right)_{i-\frac{1}{2},j}\left|\vec{S}_{i-\frac{1}{2}}\right| + \tag{9}$$
$$\frac{1}{V_{i,j}}\left(F_v S_{jxp} + G_v S_{jyp}\right)_{i,j+\frac{1}{2}}\left|\vec{S}_{j+\frac{1}{2}}\right| - \frac{1}{V_{i,j}}\left(F_v S_{jxp} + G_v S_{jyp}\right)_{i,j-\frac{1}{2}}\left|\vec{S}_{j-\frac{1}{2}}\right| + S_{i,j}$$

S_{ixp} is the unit area vector components. Equation 9 can be used to determine the inviscid flux passing perpendicularly through the surfaces $\vec{S}_{i+1/2}$ of the elementary basic volume (where the index " $i+1/2$ " is the average of i and $i+1$)

$$F_{\xi i+\frac{1}{2},j} = \left(FS_{ixp} + GS_{iyp}\right)_{i+\frac{1}{2},j} \tag{10}$$

All values are estimated at time $t = n+1$. The equation 10 is given by:

$$\Delta t \left(\frac{\partial U_{i,j}}{\partial t} \right)^n + \frac{\Delta t}{V_{i,j}} \left(F_{\xi i+\frac{1}{2},j} \left| \vec{S}_{i+\frac{1}{2}} \right| - F_{\xi i-\frac{1}{2},j} \left| \vec{S}_{i-\frac{1}{2}} \right| \right)^{n+1} + \frac{\Delta t}{V_{i,j}} \left(G_{\eta i+\frac{1}{2},j} \left| \vec{S}_{j+\frac{1}{2}} \right| - G_{\eta i-\frac{1}{2},j} \left| \vec{S}_{i-\frac{1}{2}} \right| \right)^{n+1} =$$

$$\frac{\Delta t}{V_{i,j}} \left(F_{v\xi i+\frac{1}{2},j} \left| \vec{S}_{i+\frac{1}{2}} \right| - F_{v\xi i-\frac{1}{2},j} \left| \vec{S}_{i-\frac{1}{2}} \right| \right)^{n+1} + \frac{\Delta t}{V_{i,j}} \left(G_{v\eta i+\frac{1}{2},j} \left| \vec{S}_{j+\frac{1}{2}} \right| - G_{v\eta i-\frac{1}{2},j} \left| \vec{S}_{i-\frac{1}{2}} \right| \right)^{n+1} + \Delta t S_{0i,j}^{n+1} \qquad (11)$$

The temporal linearization of the Eulerian flux is done by:

$$F_{\xi}^{n+1} = F_{\xi}^{n} + \left(\partial F_{\xi} / \partial U \right)^{n} \delta U^{n} = F_{\xi}^{n} + A_{\xi}^{n} \delta U^{n}$$

$$G_{\eta}^{n+1} = G_{\eta}^{n} + B_{\eta}^{n} \delta U^{n}, \Delta t \left(\partial U_{i,j} / \partial t \right)^{n} = \delta U_{i,j}^{n} \qquad (12)$$

The Jacobians of $F_{\xi} = A_{\xi} U$ and $G_{\eta} = B_{\eta} U$ with respect to U are represented, respectively, by A_{ξ} and B_{η}. In the ξ direction, the inviscid-flux $F_{\xi} = F_{\xi}^{+} + F_{\xi}^{-}$ is divided into two parts depending on upstream and downstream conditions. Using equation 12, the flux via the surface $\vec{S}_{i+1/2}$ can be expressed using the flux separation proposed by Steger and Warming (1979) involves evaluating the Jacobian matrices at the exact locations as U:

$$F_{\xi_{i+\frac{1}{2},j}}^{n+1} = A_{\xi_{i+\frac{1}{2},j}}^{+n} U_{i,j}^{n} + A_{\xi_{i+\frac{1}{2},j}}^{-n} U_{i+1,j}^{n} + A_{\xi_{i+\frac{1}{2},j}}^{+n} \delta U_{i,j}^{n} + A_{\xi_{i+\frac{1}{2},j}}^{-n} \delta U_{i+1,j}^{n} \qquad (13)$$

MacCormack (2003) proposes evaluating both at the identical location and alternate i and $i+1$ for the "predictor" and "corrector" evaluation, treating $G_{\eta_{i,j+1/2}}^{n+1}$ in the same way. Using $q = 0$ in predictor step, $q = 1$ in the corrector step and inversely for the following integration.

$$F_{\xi_{i+\frac{1}{2},j}}^{n+1} = A_{\xi_{i+q,j}}^{+n} U_{i,j}^{n} + A_{\xi_{i+q,j}}^{-n} U_{i+1,j}^{n} + A_{\xi_{i+q,j}}^{+n} \delta U_{i,j}^{n} + A_{\xi_{i+q,j}}^{-n} \delta U_{i+1,j}^{n} \qquad (14)$$

In boundary layers, MacCormack splitting produces good results, but it can become unstable in regions with large pressure gradients. Steger and Warming suggested an expression that is significantly more dissipative and enables the scheme's stability in these regions. In this work, we combined the two previous weight functions into one. The formula for the weight function is

$$F_{\xi_{i+1/2,j}} = W_P \left(F_{\xi_{i+1/2,j}} \right)_{McCorm} + \left(1 - W_P \right) \left(F_{\xi_{i+1/2,j}} \right)_{Steg,Warm} \qquad (15)$$

$W_P = 1 / \left(1 + \Delta P^2 \right)$ represents the function of weight connected to the pressure difference $\Delta P = \left(\bar{P}_{i+1,j} - \bar{P}_{i,j} \right) / \min \left(\bar{P}_{i,j}, \bar{P}_{i+1,j} \right)$ over two adjacent cells. Finally, the equation 11 becomes:

$$\delta U_{i,j}^{n} + \frac{\Delta t}{V_{i,j}}\left(A_{\xi_{i+\frac{1}{2},j}}^{+n}\,\delta U_{i,j}^{n} + A_{\xi_{i+\frac{1}{2},j}}^{-n}\,\delta U_{i+1,j}^{n} \right)\left|\overrightarrow{S_{i+\frac{1}{2}}}\right| - \frac{\Delta t}{V_{i,j}}\left(A_{\xi_{i-\frac{1}{2},j}}^{+n}\,\delta U_{i-1,j}^{n} + A_{\xi_{i-\frac{1}{2},j}}^{-n}\,\delta U_{i,j}^{n} \right)\left|\overrightarrow{S_{i-\frac{1}{2}}}\right|$$

$$+ \frac{\Delta t}{V_{i,j}}\left(B_{\eta_{i,j+\frac{1}{2}}}^{+n}\,\delta U_{i,j}^{n} + B_{\eta_{i,j+\frac{1}{2}}}^{-n}\,\delta U_{i,j+1}^{n} \right)\left|\overrightarrow{S_{j+\frac{1}{2}}}\right| - \frac{\Delta t}{V_{i,j}}\left(B_{\eta_{i,j-\frac{1}{2}}}^{+n}\,\delta U_{i,j-1}^{n} + B_{\eta_{i,j-\frac{1}{2}}}^{-n}\,\delta U_{i,j}^{n} \right)\left|\overrightarrow{S_{j-\frac{1}{2}}}\right|$$

$$= -\frac{\Delta t}{V_{i,j}}\left(A_{\xi_{i+\frac{1}{2},j}}^{+n}\,U_{i,j}^{n} + A_{\xi_{i+\frac{1}{2},j}}^{-n}\,U_{i+1,j}^{n} \right)\left|\overrightarrow{S_{i+\frac{1}{2}}}\right| + \frac{\Delta t}{V_{i,j}}\left(A_{\xi_{i-\frac{1}{2},j}}^{+n}\,U_{i-1,j}^{n} + A_{\xi_{i-\frac{1}{2},j}}^{-n}\,U_{i,j}^{n} \right)\left|\overrightarrow{S_{i-\frac{1}{2}}}\right| + \qquad (16)$$

$$\frac{\Delta t}{V_{i,j}}\left(B_{\eta_{i,j+\frac{1}{2}}}^{+n}\,U_{i,j}^{n} + B_{\eta_{i,j+\frac{1}{2}}}^{-n}\,U_{i,j+1}^{n} \right)\left|\overrightarrow{S_{j+\frac{1}{2}}}\right| - \frac{\Delta t}{V_{i,j}}\left(B_{\eta_{i,j-\frac{1}{2}}}^{+n}\,U_{i,j-1}^{n} + B_{\eta_{i,j-\frac{1}{2}}}^{-n}\,U_{i,j}^{n} \right)\left|\overrightarrow{S_{j-\frac{1}{2}}}\right| +$$

$$\frac{\Delta t}{V_{i,j}}\left(F_{v\xi_{i+\frac{1}{2},j}}^{n+1}\,\left|\overrightarrow{S_{i+\frac{1}{2}}}\right| + F_{v\xi_{i-\frac{1}{2},j}}^{n+1}\,\left|\overrightarrow{S_{i-\frac{1}{2}}}\right| \right) + \frac{\Delta t}{V_{i,j}}\left(G_{v\eta_{i,j+\frac{1}{2}}}^{n+1}\,\left|\overrightarrow{S_{j+\frac{1}{2}}}\right| + G_{v\eta_{i,j-\frac{1}{2}}}^{n+1}\,\left|\overrightarrow{S_{j-\frac{1}{2}}}\right| \right) + \Delta t\,S_{0\,i,j}^{n+1}$$

A parallel implicit finite volume Fortran code based on full Navier-Stokes unsteady equations is developed to solve axisymmetric nozzle flows using RSM-Omega turbulence model, the numerical technic and validation via SST turbulence model is well described in reference Bensayah et al. (2014).

3. Findings and discussion

To understand what actually happens in TOC nozzles, several experimental studies, carried out on optimized nozzles with subscale (Nave and Coffey (1973), Nguyen et al. (2003), Hadjadj et al. (2015) and Ijaz Rajesh (2019)) or full-scale (Nave and Coffey (1973)), confirmed by various numerical simulations (Frey and Hagemann (1998), Aghababaie and Theunissen (2015), Maicke et al. (2013)) and experiments (Frey et al. (2017), Meng and Ye (2017), Changsoo et al. (2020), Martelli et al. (2020), Ruyan et al. (2016)), and Stark Genin (2016), have an FSS separation kind, the flow boundary layer separated from the nozzle wall and is not reattached (see Fig. 3a), while a restricted shock separation is marked by closed recirculation bubbles that are re-attached to the wall nozzle behind the point of separation (see Fig. 3b), interaction of boundary layers and shock waves that takes place in significantly over-expanded nozzles may exhibit considerable instability that leads to symmetrical or asymmetrical flow separation, according to a number of prior studies on supersonic nozzles (Lawrence (1967) and Verma (2002)). Shock-induced separation is not desired in rocket design because asymmetry in the flow might result in damaging lateral forces. A number of viscous phenomena, such as adverse pressure gradients boundary layers, shear layers, recirculation bubble zones, and shock-induced separation can occur and significantly impact the flow field in the nozzle. For the purpose of predicting the switch from FSS to RSS, Ostlund and Bigert (1999) and Hadjadj et al. (2015) presented a reasonable empirical criterion that links the FSS to RSS switch to an axial location at which the moderate centerline normal shock corresponds with the RSS front separation.
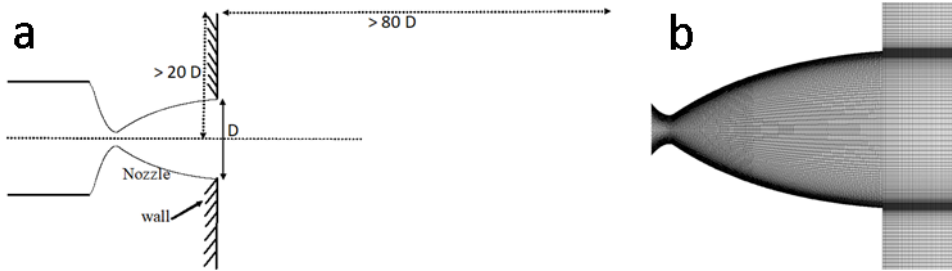
Fig. 1. (a) Geometric configuration of simulated nozzle, (b) Computational grid for LEA-TOC nozzle.

3.1 Free shock separation (FSS)

The separation in initiated nozzle takes place in the divergent upstream of the lip nozzle due to the presence of adverse pressure gradients, and the free-flowing jet emerges in atmosphere at rest, the boundary-layer separates and extends freely to the outlet lip of the nozzle. The static wall pressure at the outlet is often slightly less than the ambient pressure (Fig. 2a and 2b), the first deviation in the wall pressure is called the beginning separation pressure (Pi). The wall pressure then increases rapidly to a so-called plateau pressure (Pp), which is generally below atmospheric pressure (Pa).

The increase in pressure between (Pp) and (Pa), due to the recirculation zone, is much less marked. Free separation is shown schematically in Figs. 3a, 2a and 2b. It involves two distinct zones; one is governed by the jump of the pressure (Pi/Pp) and the other by the jump (Pp/Pa) related to the ambient flow aspirated in the region of recirculation (back flow). A compression is exerted on the boundary layer of the jet where a shock is formed at the first point of increasing wall pressure just upstream of the detachment point. The adverse pressure gradient at this point does not reach the value necessary for boundary layer separation and does not allow the back flow to penetrate inside the nozzle. Consequently, the flow continues to expand until the separation point, where the intensity of the shock becomes increasingly large and sufficient to cause the separation of the boundary layer. The wall pressure distribution in this case is undisturbed, reaching an asymptote (NPR = 15; 16) corresponding to the plateau pressure (Pp) characteristic of the extended flow, the pattern obtained corresponds to a Mach reflection.
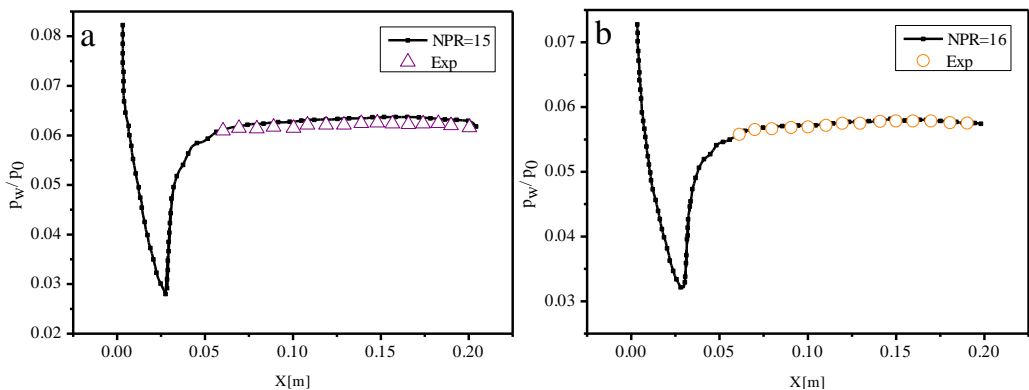

Fig. 2. Comparison between experimental data (Nguyen et al. 2003) and computation for the mean static wall pressure, TOC nozzle at (a) NPR=15, (b) NPR=16.

The type of reflection strongly depends on the stagnation pressure ratio (NPR) and wall contour of the nozzle. However, the transition between these reflections may involve a hysteresis effect (Zmijanovic et al. (2012)), Aghababaie & Theunissen (2015) and Maicke et al. (2013). In FSS separation the incident shock (I) is reflected by forming a normal shock to the axis called the Mach disc (Fig. 3a-top). The triple point (TP), or meet the reflected shock, the incident shock and the Mach disc, emanates a slip line (SL). This isobaric discontinuity separates the subsonic pocket downstream from the strong shock of the supersonic zone downstream of the reflected shock (r). The other called "singular" or "Mach", where the incident shock (I) is reflected by forming a normal shock to the axis called the Mach disc (Fig. 3a-bottom). When the profile of the nozzle is highly optimized in thrust (TOC and TOP), an internal shock (IS) is then formed. Interference of the incident shock (I) with the internal shock can lead to a complex structure of shock called "cap-shock" (Fig. 3b). Figures 2a and 2b with NPR=15 and 16 show a comparison of numerical findings with experimental data. The computed wall static pressure agrees well with the experimental measurements, the level of plateau pressure is well calculated and this level decreases with increasing stagnation pressure (NPR).

3.2 Restricted shock separation (RSS)

Regular reflection (RR) and Mach reflection (MR) can be detected in the plumes of all kinds of nozzles, whereas the cap shock structure only exists for nozzles having internal shock, which include ideal optimized truncated nozzles. Transition of the cap shock structure to Mach or regular reflection is determined by the form of the contour and the operating conditions of the nozzle chamber. In addition, substantial hysteresis was detected for the NPR pressure ratio during the transition from nozzle startup and for the shutdown operation. Fig. 3b shows the confrontation between the schematic illustration and the numerical prediction of the cap-shock structure presented in the form of a schlieren picture; in this situation, the structure of the cap shock is often created by the internal shock (i1) impacting with the incoming center Mach disc (MD1). Reflected shock (r1) produced by the interaction is subsequently confronted to the incident-shock (i2) and forms a regular reflection (r2). The FSS exist only with NPR < 24, when increasing pressure than the typical RSS flow separation developed unexpectedly under NPR > 24. The obtained RSS flow patterns have three to four smaller pressure peaks with NPR = 24.9 additional to the strong peak set near the location of flow detachment. The peaks of pressure are stable and do not vary under the same NPR and shift somewhat with the change in stagnation pressure. This structure was reported in the early 1970s by Nave and Coffey (1973), suggesting a transition in the separation of FSS to RSS and vice-versa. However, it was not understood that these transitions were responsible for the two distinct lateral load peaks until Mattsson et al. (1999) presented a detailed analysis of the flow of the VOLVO S1 nozzle. The calculation of Chen et al. (1994) showed behind the recompression shock a formation of a trapped vortex, in the simulation of the flow reattachment in the J-2S subscale engine. Hereafter, Nasuti and Onofri (1996, 2009) pointed out that lateral load generation is mainly caused by the centerline vortex and provided a probable interpretation for its origin largely due to the essential role of the upstream flow gradient of the Mach disc in the core of the nozzle (see Fig. 3c). From this explanation, a non-viscous mechanism may be the main cause of the vorticity generation.
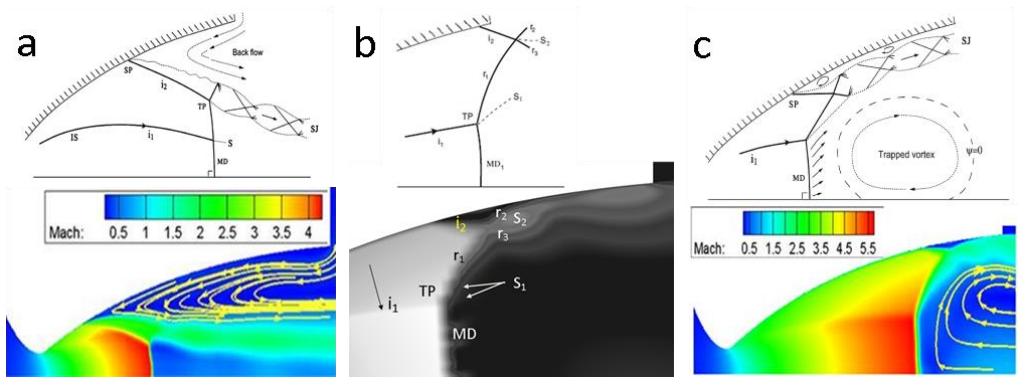
Fig. 3. (a) Free Shock Separation, (Top) Schematic of high-area-ratio and (Bottom) numerical simulation in LEA-TOC with NPR=15, SJ supersonic jet, SP separation point, IS internal shock, r reflected shock; (b) Confrontation of Schematic representation of cap-shock structure and shock interactions in over-expanded supersonic nozzles in the theoretical case (top) and numerical simulation (bottom) i1 internal shock, TP triple point, r reflected shock, S slip-line, i2 incident shock; (c) Restricted Shock Separation, (Top) A schematic of high-area-ratio with RSS separation pattern and (bottom) numerical result with NPR=25.

The incident flow irregularities on the Mach disc, in fact, play a crucial and determining role. Owing to the non-uniform flow upstream, and the relatively uniform pressure downstream, the impact shock on its surface cannot be constant, and its form assumes a curved contour instead of a flat one. As a result, downstream the Mach disc, a rotational flow with speed gradients and entropy occurs, which amplifies to increase the irregularity of the flow upstream and generates vertical patterns.

The vortex centerline, with size and growing rate are primarily managed by viscous factors, serves as an obstacle for the main evacuation jet, which then deflects towards the wall. Consequently, behind the shock a radial flow is developed, which tries to attach the detached zone to the wall, thereby changing the flow pattern of the detached zone from FSS to RSS. Downstream the point of reattachment and owing to the impact of the flow on the wall, the pressure suddenly increases (see Fig. 4).
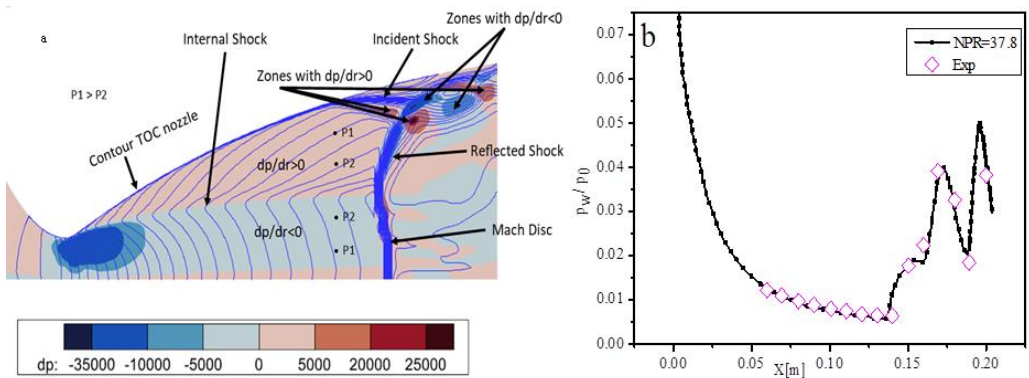

Fig. 4. (a) Mach number (blue lines) and radial Pressure gradient ($\partial p/\partial r$) contour computed at NPR=25 for LEATOC nozzle, (b) Wall pressure ratio for LEA-TOC nozzle for startup at NPR=37.8, Exp (Nguyen et al. 2003).

The flow inside the diverging portion of the nozzle is typically partitioned into three areas: the core, the radial gradients, and the uniform flow zones. In TOC nozzles, compressional waves originate from the inflection point, gather and generate a weak shock called internal shock. The nozzle flow usually has a radial pressure gradient $\partial p / \partial r$, that can either be positive or negative. The TOC nozzle core has a negative pressure gradient of $\partial p / \partial r < 0$ (see Fig. 4a). This negative gradient of pressure provokes the Mach disk to bend backward when it is pushed radially outward, backward when it is moved radially outward as indicated by Nasuti and Onofri (2009). A sudden pressure jump is induced through the internal shock, and then the pressure stabilizes. Thereafter, the pressure progressively increased until it attained the wall of the nozzle. This positive pressure variation in the radial outward direction provokes the Mach disk to bend forward when pushed radially outward, leading to a type 2 Mach reflection with non-uniform flow. Fig. 2a depicts the pressure gradients within the nozzle and the patterns of shock caused by the non-uniformities in the upstream flow. In Fig. 4b a comparison is made between the normalized wall pressure (pw) to the inlet stagnation pressure (p0), using the MacCormack scheme with NPR = 37.8, showing a very good agreement of numerical predictions and the experiment data (Nguyen et al. 2003), in this distribution, the pressure peaks are well captured, except in the region of the nozzle lip, this may be due to differences between numerical and experimental configurations, and the complexity of shock boundary interaction, so it is often difficult to capture well all the details even with the use of very sophisticated methods. Fig. 5a shows the hysteresis phenomenon, in which the transition between FSS-RSS occurring in the nozzle at the start and end of the rocket engine is displayed differently.
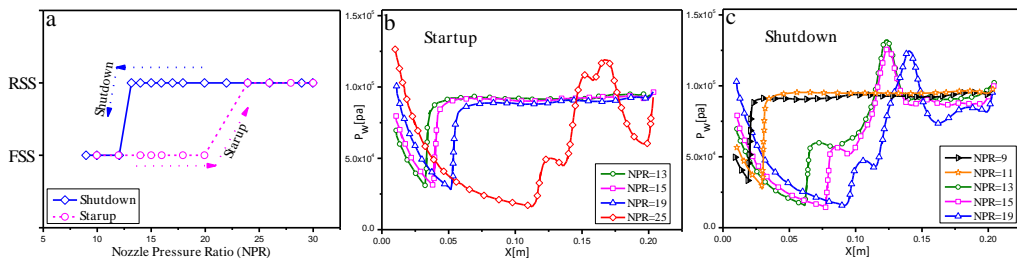

Fig. 5. (a) Hysteresis cycle of LEA-TOC in the present study, Static wall pressure distribution during the (b) startup and (c) shutdown process.

The objective is to numerically re-capture the hysteresis observed in experimental studies, including regular and Mach interactions. The effect of hysteresis is clear from the findings of the calculation analysis. At the startup process, the FSS to RSS switch occurs at NPR > 24 (see Fig. 5b), and RSS to FSS re-transition during shutdown occurs at NPR < 13 (see Fig. 5c). It can be observed that during the shutdown process when NPR > 30, the location of the RSS separation flow moved upstream at about the similar rate as it moved down-stream during the startup process.

Calculations of the wall static pressure during shutdown indicate that the switch from RSS to FSS occurs at lower stagnation pressure ratio (NPR). The principal difference is that the line of the FSS separation is situated much more upstream of the RSS separation line because of the reattachment of the flow to the wall, and a close recirculating bubble is created, with static pressure much lower than the atmospheric pressure. Therefore, the separation line jumps when a transition from FSS-to-RSS or RSS-to-FSS occurs. The FSS plateau pressure is quite near to atmospheric pressure, but the plateau pressure for RSS is often significantly lower; the hysteresis may be described partially by the smaller plateau pressure (see Fig. 6) in the confined recirculating bubbles compared to the FSS scenario.
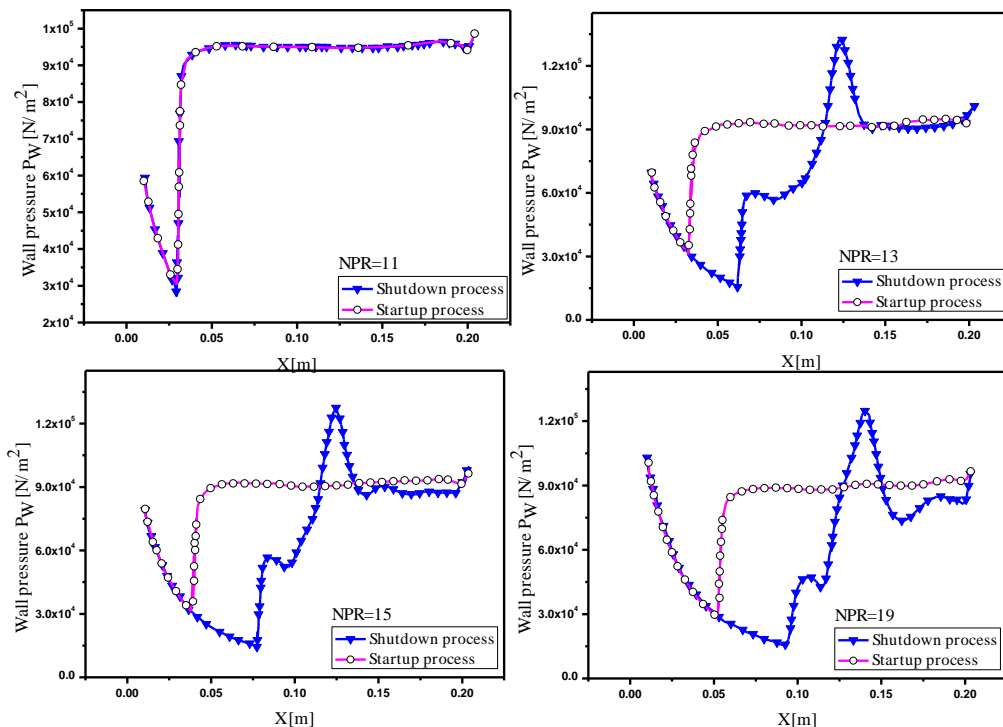
Fig. 6. Comparison of startup and shutdown wall plateau pressure distribution.

4. Conclusions

This study reports the results of numerical simulations of compressible nozzle flows using the Omega Reynolds stress turbulence model and the MacCormack implicit numerical scheme. The numerical findings were compared with the available experimental data, and the qualitative agreement was generally quite good. In the second part, we proceed to a more complex shock-wave/boundary-layer interaction, in which the shock pattern can be more dramatic because of the rapid expansion of the optimized wall contour. For free separation shock (FSS), the findings are in excellent agreement with the measurements; this type of shock is well-captured in detail. For restricted separation, the results obtained showed very satisfactory agreement with the existing complex phenomena, which provided details on the behavior of the flow structure. The numerical scheme and turbulence model demonstrated their capability to reproduce the hysteresis phenomenon during the FSS-RSS transition, with both solutions obtained at the same stagnation pressure ratio (NPR) as a function of the starting conditions. This hysteresis is attributed to the fact that the plateau pressure in the FSS regime is higher than that in confined recirculating bubbles. Consequently, the same nominal NPR corresponds to two distinct plateau pressure ratios with two distinct abscissa values of the detachment point: the first in the FSS domain and the second in the RSS domain. The results show that the numerical scheme with the use of a combined weight function for flux splitting and the Omega-RSM model presented here are promising tools for predicting the complex behavior of the boundary layer shock wave interactions.

References

Aghababaie A.A., Theunissen R (2015). Modeling Free Shock Separation Induced Side Loads in Overexpanded Rocket Nozzles, AIAA Journal, 53(1),93–103.https://doi.org/10.2514/1.J053014.

Bensayah K., Hadjadj A., Bounif A (2014). Heat Transfer in Turbulent Boundary Layers of Conical and Bell-Shaped Rocket Nozzles with Complex Wall Temperature, Numerical heat transfer-part A, 66(3),289-314. http://dx.doi.org/10.1080/10407782.2013.873283.

Changsoo L., Kyungjun C., Chongam K., Sanghoon H (2020). Computational investigation of flow separation in a thrust-optimized parabolic nozzle during high-altitude testing, Computers and Fluids, 197, 104363. https://doi.org/10.1016/j.compfluid.2019.104363.

Chen C.L., Chakravarthy S.R., Hung C.M (1994). Numerical investigation of separated nozzle flows. American Institute of Aeronautics and Astronautics, 32(9), 1836–1843. https://doi.org/10.2514/3.12181.

Frey M., Hagemann G. (1998). Status of Flow Separation Prediction in Rocket Nozzles. American Institute of Aeronautics and Astronautics, 98-3619. https://doi.org/10.2514/6.1998-3619.

Frey M., Makowka K., Aichner T (2017). The TICTOP nozzle: a new nozzle contouring concept, CEAS Space J 9, 175–181. https://doi.org/10.1007/s12567-016-0139-z.

Hadjadj A., Perrot Y., Verma S (2015). Numerical study of shock/boundary layer interaction in supersonic overexpanded nozzles, Aerospace Science and Technology, 42, 158-168. http://dx.doi.org/10.1016/j.ast.2015.01.010.

Ijaz M., Rajesh G (2019). Shock Interactions in Thrust Optimised Parabolic (TOP) Nozzles during Start-Up and Shutdown, 31st International Symposium on Shock Waves 2. Springer, Cham. https://doi.org/10.1007/978-3-319-91017-868.

Lawrence R.A (1967). Symmetrical and unsymmetrical flow separation in supersonic nozzles, Southern Methodist Univ Dallas TX United States, RR-67-1, NASA-CR-92587.

MacCormack R.W (2003). The Effect of Viscosity in Hypervelocity Impact Cratering, Journal of Spacecraft and Rockets, 40(5), 757-763. https://doi.org/10.2514/2.6901.

Maicke B.A., Majdalani J., Geisler R.L (2013).Characterization of the startup and pressure blowdown processes in rocket nozzles, Aerospace Science and Technology, 25(1), 273-282. https://doi.org/10.1016/j.ast.2012.02.003.

Martelli E., Saccoccio L., Ciottoli P., Tinney C., Baars W., Bernardini M (2020). Flow dynamics and wall-pressure signatures in a high-Reynolds-number overexpanded nozzle with free shock separation, Journal of Fluid Mechanics, 895, A29. doi:10.1017/jfm.2020.280.

Meng X., Ye Z (2017). The transition of flow pattern and the influence of outflow on flow pattern in over-expanded rocket nozzle, 53rd AIAA/SAE/ASEE Joint Propulsion Conference, https://doi.org/10.2514/6.2017-5067.

Mattsson J., Hogman U., Torngren L (1999). A Sub-Scale Test Programme on Investigation of Flow Separation and Side-Loads in Rocket Nozzles, Proceedings of the 3rd European Symposium on Aerothermodynamics of Space Vehicles, ESA-ESTEC. Bibliographic Code: 1999 ESASP.426..373M.

Nasuti F., Onofri M (2009). Shock structure in separated nozzle flows. Shock Waves, 19, 229–237. https://link.springer.com/article/10.1007/s00193-008-0173-7.

Nasuti F., Onofri M. (1996). Viscous and Inviscid Vortex Generation During Nozzle Flow Transients. 34th AIAA Aerospace Sciences Meeting and Exhibit, AIAA paper, 96-0076. https://doi.org/10.2514/6.1996-76.

Nave L.H, Coffey G.A (1973). Shock Sea-level side loads in high-area-ratio rocket engines, AIAA J 73-1284, 1-65.

Nguyen A.T., Deniau H., Girard S., Alziary de Roquefort T (2003). Unsteadiness of flow separation and end-effects regime in a thrust-optimized contour rocket nozzle, Flow

Turbulence and Combustion, 71, 161-181. https://link.springer.com/article/10.1023/B:APPL.0000014927.61427.ad

Ostlund J., Bigert M (1999). A Subscale Investigation on Side Loads in Sea Level Rocket Nozzles, 35th Joint Propulsion Conference and Exhibit, AIAA Journal, 99-2759. https://doi.org/10.2514/6.1999-2759

Ruyan J., Zhenyu J., Weihua Z (2016). Transient three-dimensional side-loads analysis of a thrust-optimized parabolic nozzle during staging, Acta Astronautica, 122, 137-145.https://doi.org/10.1016/j.actaastro.2016.01.023.

Stark R., Génin C (2016). Optimization of a Rocket Nozzle Side Load Reduction Device. Journal of propulsion and power, 32(6), 1395-1402.https://doi.org/10.2514/1.B35971.

Steger J.L., Warming R.F (1979). Flux Vector Splitting of the Inviscid Gas Dynamics Equations with application to Finite Difference Methods, NASA Technical Memorandum 78605.

Wang T.S., Lin J., Guidos M. (2013). Transient Side-Load Analysis of Out-of-Round Film-Cooled Nozzle Extensions. Journal of Propulsion and Power, 29(4), 855–866. DOI:10.2514/1.B34812

Verma S.B (2002). Study of flow separation in truncated ideal contour nozzle, Journal of Propulsion Power, 18(5), 1112–1121. https://doi.org/10.2514/2.6042.

Zmijanovic V., Rasuo B., Chpoun A (2012). Flow Separation Modes and Side Phenomena in an Overexpanded Nozzle, FME Transactions, 40(3), 111-118. https://scindeks.ceon.rs/article.aspx?artid=1451-20921203111Z